Ca-repaired $BaZrO_3$ nanorods/$YBa_2Cu_3O_{7-x}$ interface for enhanced pinning in $YBa_2Cu_3O_{7-x}$ nanocomposites with 2-8% $BaZrO_3$ doping

Judy Wu[*1], Mohan Panth[1], Victor Ogunjimi[1], Mary Ann Sebastian[2,3], Di Zhang[3], Timothy Haugan[2], Haiyan Wang[4]

[1]*Department of Physics and Astronomy, the University of Kansas, Lawrence, Kansas 66045, USA*
[2]*U.S Air Force Research Laboratory, Aerospace Systems Directorate, WPAFB, OH 45433, USA*
[3]*University of Dayton Research Institute, Dayton, OH 45469, USA*
[4]*School of Materials Engineering, Purdue University, West Lafayette, IN 47907, USA*
*Corresponding author e-mails: jwu@ku.edu

Abstract: C-axis aligned $BaZrO_3$ (BZO) nanorods formed via strain-mediated self-assembly in BZO-doped $YaBa_2Cu_3O_{7-x}$ (BZO/YBCO) nanocomposite films can provide strong pinning to the quantized magnetic vortices. While the strain initiated from the BZO/YBCO lattice mismatch plays a critical role in nucleation and evolution of the BZO nanorods, it also leads to a highly defective BZO/YBCO interface and hence reduced pinning efficiency of BZO nanorods. This work reports a recent study in probing the effect of BZO/YBCO interface on the pinning efficiency of the BZO nanorods as the interface is repaired dynamically during the BZO nanorod growth using Ca doping. Within the BZO doping range of 2-8 vol.%, significantly enhanced pinning efficiency of the BZO nanorods have been observed. A peak enhancement up to five-fold of critical current density at 9.0 T and 65-77 K has been obtained in the 6 vol.% BZO/YBCO nanocomposites after the interface repair. This result not only illustrates the critical importance of the BZO/YBCO interface in the pinning efficiency, but also provides a facile scheme to achieve such an interface to restore the pristine pinning efficiency of the BZO nanorods.

Keywords: YBCO nanocomposite film, artificial pinning center, vortex pinning efficiency, coherent interface, dynamic lattice enlargement

1. Introduction:

Enhancing pinning of quantized magnetic vortices in high temperature superconductors (HTSs) has been the focus of applied superconductivity research in last few decades to meet the requirement of high higher critical current density (J_c) in applied magnetic fields (B) in many applications ranging from power transmission cables, high field magnets, etc. Most HTSs have growth defects that can provide pinning typically in low magnetic fields. In order to achieve high J_c (B) at larger B fields of a few to tens of Tesla, more recent effort in vortex pinning has been focused on generation of so-called artificial pinning centers (APCs) through doping of impurities that may self-assemble into nanoscale precipitates in HTS matrix, such as $YBa_2Cu_3O_{7-x}$ (YBCO). In physical vapor deposition (PVD) such as pulsed laser deposition (PLD), such an APC self-assembling is driven by the strain field initiated from the interface between the APC/YBCO due to the lattice mismatch. An elastic strain energy model of such a PVD process has revealed that the strain field plays a critical role in determining APC's morphology, dimension, concentration and orientation [1-3]. In particular, vertically aligned arrays of one-dimensional (1D) APCs or nanorods can form in the c-axis-oriented YBCO films and coated conductors through the film thickness. Many impurities have been reported to form 1D-APCs in YBCO including $BaZrO_3$ (BZO) [4-8], $BaSnO_3$ [9, 10], $BaHfO_3$ (BHO) [11-15], $YBa_2(Nb/Ta)O_6$ [16, 17]. These 1D-APCs can provide a strong collective pinning at B//c-axis to address the weak pinning issue associated to the layered structure of YBCO.

Despite the important role of the strain field in self-assembly of 1D-APCs, the large lattice mismatch at the 1D-APC/YBCO interface can result in a high interface defect density [18-20] and hence reduced superconductivity due to oxygen deficiency [21]. Because the specific pinning force density

(F_p) of 1D-APCs is proportional to the radial derivative of the pinning energy at the 1D-APC/YBCO interface [22], a degraded pinning efficiency of 1D-APCs is anticipated [21] and confirmed experimentally through a comparison between BZO (defective interface) and BHO (less defective coherent) from the pinning performance in the latter [19, 23, 24]. In order to reduce the interface defects on the BZO 1D-APC/YBCO interface, we recently developed a multilayer (ML) approach for reduction of the BZO/YBCO lattice mismatch via enlarging the c-axis constant of YBCO locally around the BZO 1D-APCs [25]. Specifically, two Ca-containing thin spacer layers of 5-10 nm in thickness were grown with BZO/YBCO layers in the ML structure to allow Ca diffusion into BZO/YBCO layer from the spacers after the BZO 1D-APCs are formed. The purpose of the ML approach is to promote Ca/Cu replacement while prevent Ca/Y and Ca/Ba replacements on the YBCO lattice. It should be noted that the formed BZO 1D-APC/YBCO interface experiences a large tensile strain since BZO lattice is ~7.7% larger than the c-axis lattice constant of YBCO. The replacement of smaller Cu+2 ions on the Cu-O planes of YBCO lattice with larger Ca+2 ions (by 30%) would be energetically favorable [25, 26]. This hypothesis of an enlarged YBCO's c-axis lattice constant has been confirmed in the BZO/YBCO ML samples to allow a coherent BZO 1D APC/YBCO interface to form [25]. This suggests the Ca cation replacement is strain-dependent, which was predicted in a theoretical simulation on the Ca-doping effect of YBCO bulks [27].

While improved pinning has been observed on 2 and 6 vol.% BZO/YBCO ML samples, many questions remain on the microscopic mechanism of Ca diffusion and its correlation with the strain field in BZO/YBCO. In order to shed light on this important matter, this work explores perturbance of the strain field in BZO/YBCO through varying the BZO doping in the range of 2-8 vol.% and addition of a secondary impurity of Y_2O_3 of 3 vol.%. Through investigation of superconducting properties of these samples, we aims to achieve an understanding of the effect of Ca on the pinning properties of the BZO/YBCO nanocomposite films.

2. Experimental

PLD was applied to prepare four sets of samples on (100) $SrTiO_3$ (STO) single crystal substrates [4, 28, 29]. The PLD targets of BZO doped YBCO with the BZO doping of 2-8 vol.% were used. Two sets of the samples were made single-layer (SL) either with single-doping (SD) of BZO (BZO/YBCO SD-SL) or with an additional 3 vol.% of Y_2O_3 (BZO/YBCO DD-SL). Another two sets of ML samples are otherwise the same except containing two additional 10 nm thick $Ca_{0.3}Y_{0.7}Ba_2Cu_3O_{7-x}$ (CaY-123) spacers inserted in the SL samples, dividing the BZO/YBCO SD-SL or BZO/YBCO DD-SL into three layers each having the same thickness. For convenience, they are regarded as BZO/YBCO SD-ML or BZO/YBCO DD-ML, respectively. The CaY-123 spacers were deposited *in situ* with the BZO/YBCO or BZO-Y_2O_3/YBCO layers. The PLD repetition rate was 2 Hz and 8 Hz respectively for the CaY-123, and for BZO/YBCO or BZO-Y_2O_3/YBCO layers. The PLD was performed in 300 mTorr O_2 at a substrate temperature of ~825 °C for all samples [4]. Immediately after the PLD deposition, the samples were cooled to 500 °C in one atmosphere O_2 pressure and annealed for about 30 minutes before further cooling down to room temperature. The film thicknesses of 150-160 nm were measured using a Tencor P-16 profilometer on all samples. Ag contact pads of ~ 100 nm in thickness were sputtered on the freshly made samples to achieve low contact resistance. Standard photolithography was used to pattern two microbridges of length ~500 μm and widths of 20 and 40 μm respectively. The details of the photolithography and sample wiring for the transport measurement can be found in our previous papers [30, 31]. The samples were mounted on a oxygen-free Cu stage using Ag paste and resistance–temperature (*R-T*) and current-voltage (*I-V*) characteristic curves were measured as function of temperature *T* (65K-77 K) and the magnetic field *B* (up to 9.0 T) applied in the c-axis of the BZO/YBCO films in a Quantum Design Ever-Cool II Physical Property Measurement System (PPMS). To prevent damage of the samples at high applied currents in the *I-V* measurement, a pulsed current source (Keithley 2430 Pulse Source Meter) was utilized with the pulse width of ~ 500 ms. J_c was determined by applying 1 μV/cm standard criterion.[31-33]

3. Results and Discussions

Figure 1 illustrates schematically the microstructures of the four sets of samples of (a) BZO/YBCO SD-SL, (b) BZO/YBCO SD-ML, (c) BZO/YBCO DD-SL, and (d) BZO/YBCO DD-ML, respectively. In

the BZO/YBCO SD-SL samples (Figure 1a), BZO is the only doped impurity and forms c-axis aligned 1D-APCs (black lines) along the normal direction of the film. Since BZO has a larger lattice constant by 7.7% than the c-axis lattice constant of YBCO, a tensile strained YBCO around the BZO 1D-APC is present as shown schematically by the green columns around the BZO 1D-APCs. This modulated strain field plays a critical role in self-assembly of the BZO 1D-APCs during the sample growth. With increasing BZO doping, the diameter of the BZO 1D-APC remains almost a constant at ~ 5-6 nm, while the spacing between the BZO 1D-APCs decreases monotonically [4, 19, 34] from ~ 20 nm at 2 vol.% to <10 nm at 8 vol.%. The strain field overlap at larger BZO doping would impact the superconductivity of YBCO negatively illustrated in the decrease of the T_c values of BZO/YBCO SD

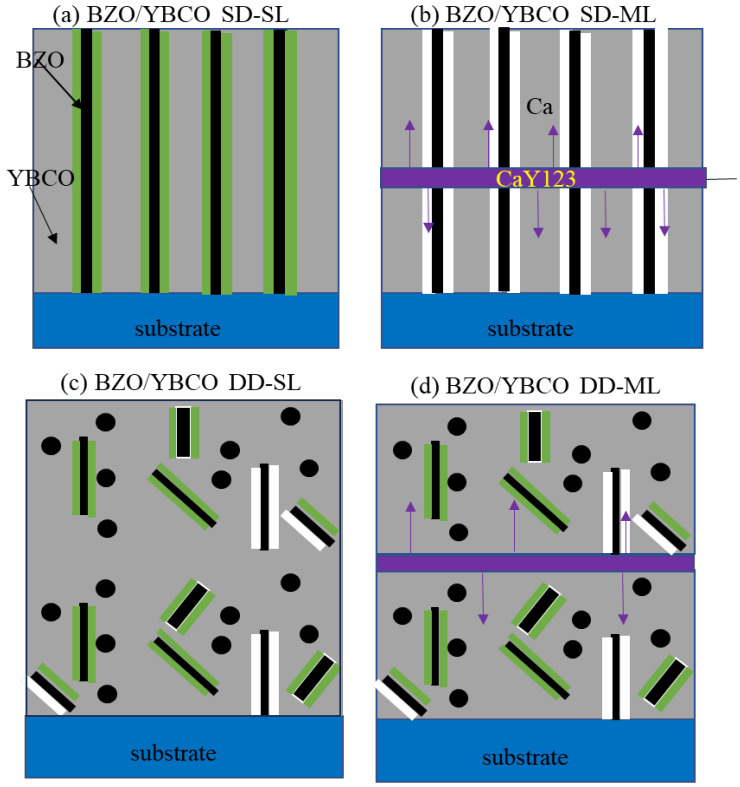

Figure 1. Schematic diagrams of (a) BZO/YBCO SD-SL, (b) BZO/YBCO SD-ML, (c) BZO-Y_2O_3/YBCO DD-SL and (d) BZO-Y_2O_3/YBCO DD-ML nanocomposite films

SL samples, which in turn reduces the J_c the values at temperatures close to T_c values such as 77 K. In order to reduce or eliminate the negative effect of the strain field while not to disturb its role in self-organization of BZO 1D-APCs, Ca diffusion from the CaY-123 spacers into the bottom and top BZO/YBCO layers has been explored in the BZO/YBCO SD-ML samples (Figure 1b). Note the BZO 1D-APCs in the first BZO/YBCO layer in the ML sample forms in the identical way to that in the SL case with the same diameter and concentration. The Ca diffusion from the CaY-123 spacer into the BZO/YBCO layers would then be affected by the strain field in this layer. In particular, the tensile strain at the BZO/YBCO interface would facilitate Ca diffusion along the interface (purple arrows in Figure 1b) followed with energetically favorable Ca/Cu replacement on the Cu-O planes of YBCO to reduce the tensile strain since Ca ion is ~30% larger than the Cu ion. This results in enlarged c-axis lattice constant of YBCO from the original 1.17 nm to 1.24 nm and hence reduced BZO/YBCO interface lattice mismatch from 7.7% to 1.4% [25, 26]. The resulted coherent interface is shown schematically as the white columns around the BZO 1D-APCs in Figure 1b. In the BZO/YBCO DD-SL case (Figure 1c), the modulated strain field is much reduced by the presence of the Y_2O_3 nanoparticles due to the local strain perturbation especially when strain overlap is the case at high BZO doping above 2 vol.% [31, 35]. The immediate consequence is the truncated BZO 1D-APCs into short segments with a fairly large range of alignments. As the CaY-123 spacers are introduced in the BZO/YBCO DD-ML samples

(Figure 1d), the Ca diffusion would be considerably affected. In particular, the tensile-strain directed Ca diffusion along the BZO 1D-APC/YBCO interface may no longer be a dominant pathway.

Figure 2 shows the T_c *vs* BZO doping curves measured on the four sets of samples of BZO/YBCO SD-SL (black), BZO/YBCO SD-ML (red), BZO/YBCO DD-SL (blue), and BZO/YBCO DD-ML (purple). A monotonic decreasing trend can be observed on the T_c *vs* BZO doping curve for BZO/YBCO SD-SL samples from 89.2 K at for 2% BZO/YBCO SD-SL to 86.5 K for the 8% BZO/YBCO SD-SL sample. The larger T_c drop at higher BZO doping may be attributed to the more intensive strain field overlap as the spacing between the BZO 1D-APCs reduces to <10 nm. The 2-8% BZO/YBCO SD-ML samples exhibit a similar trend of T_c *vs* BZO doping up to 6% BZO doping except the decrease is slightly more, indicative a secondary mechanism of possible over-doping of YBCO by Ca. The T_c for the 6% BZO/YBCO SD-ML sample is 84.0 K, which is 2.9 K lower its SL counterpart's. Interestingly, the T_c for the 8% BZO/YBCO SD-ML sample is 85.5 K, reducing the gap with its counterpart's to ~1.0 K. This may be explained by competition for Ca between diffusion via BZO/YBCO interface, which is more at higher BZO doping and the other diffusion pathways such as Ca/Y substation (leading to T_c reduction), which may be less when the entire YBCO is under tensile strain due to increased stain field overlap at a higher BZO doping. In contrast, the T_c *vs* BZO doping curves for the BZO/YBCO DD-SL and BZO/YBCO DD-ML exhibit an opposite trend of more T_c reduction at lower BZO doping. Based on the mixed APC structure which becomes more at higher BZO doping and therefore reduces the overall modulated strain when BZO 1D-APCs become segmented and random in orientation, the strain field reduction may explain the higher T_c values at higher BZO doping. However, the overall lower T_c values in the ML samples than their SL counterparts may be associated with the Ca-overdoping of the YBCO. Nevertheless, the minimum T_c value for all four sets of samples is around 84.0 K, which may impact the comparison of J_c (*B*). To minimize the impact of T_c value, all comparisons of J_c (*B*) are selected at 65 K in the following.

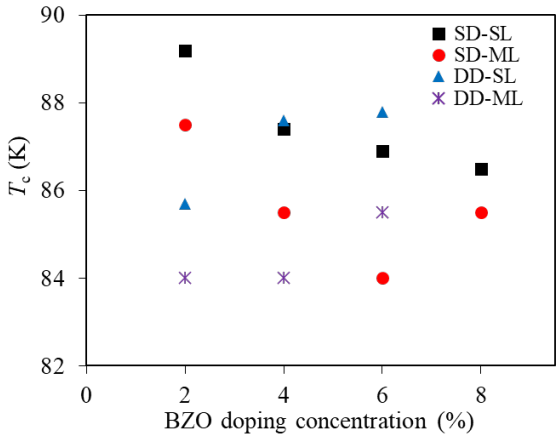

Figure 2. T_c vs BZO doping of 2-8 vol.% BZO/YBCO SD-SL (black square), SD-ML (red circle), DD-SL (blue triangle) and DD-ML (purple star) films.

Figure 3 shows the J_c (*B*) and F_p (*B*) curves measured on the four sets of samples at 65 K. The J_c (*B*) of SD films are compared in Figure 3a for 2-8 % BZO/YBCO SD-SL (open) and BZO/YBCO SD-ML (solid) at *B*//c. At all different BZO doping, the ML samples have higher J_c (*B*) than their SL counterparts in the entire *B* field range > 1.0 T. It should be noted that the BZO 1D-APCs in the ML are segmented by the CaY123 spacers but the relative thinness (~ 10 nm) with reduced pinning force per APC length as reported in multilayer YBCO structures with much thicker YBCO spacers [36-38]. The higher J_c (*B*) in the ML samples suggest this negative effect may be outweighed by the benefit of much reduced defects at the BZO/YBCO interface and the resulted YBCO lattice distortions [25]. This distortion in the YBCO lattice of SL film, which have been reported previously [39-43], arises from the strain around BZO/YBCO interface as a result of the ~ 7.7% BZO/YBCO lattice mismatch. The elimination of these defects in the ML may be attributed to the dynamic elongation of the c-axis of YBCO axis as stacking faults formed in the Ca rich region near the BZO/YBCO interface of the ML

film. The formation of the stacking faults, via Ca/Cu replacement, locally extends the YBCO c-lattice parameter thereby reducing the BZO/YBCO lattice mismatch around the BZO/YBCO interface and hence the interfacial strain. In DD case, this benefit is only limited to low BZO doping of 2 vol.% as shown in Figure 3b since the modulated strain field is not longer the case in facilitating Ca diffusion along the BZO/YBCO interface. On the other hand, the Ca-overdoping of YBCO further reduces the T_c of the BZO/YBCO DD-ML (solid). The similar trends of the F_P (B) curves in the SD and DD samples are shown in Figures 3c-d, respectively. In the former, higher F_P (B) can be observed in the 2-8% BZO/YBCO SD-ML (solid) than their SL counterparts'. The peak F_P ($F_{p,max}$) of ~ 97.7 GNm^{-3} for the 2% ML sample at 65 K is 1.7 times of the F_{pmax} of ~ 57.1 GNm^{-3} in the 2% SL sample and surpasses the ~ 80 GNm^{-3} of the 2% BHO-YBCO SL sample [19]. It should be noted that the F_{pmax} values for the 2% SL sample are comparable to that reported in literature [8, 44-46]. The highest enhancement is on 6% BZO/YBCO SD-ML with the peak $F_{p,max}$ ~ 158 GN/cm^3, which is a factor of five than its SL counterpart's. In the DD case, only moderate enhancement of F_P (B) was observed on 2% BZO/YBCO DD-ML (Figure 3d).

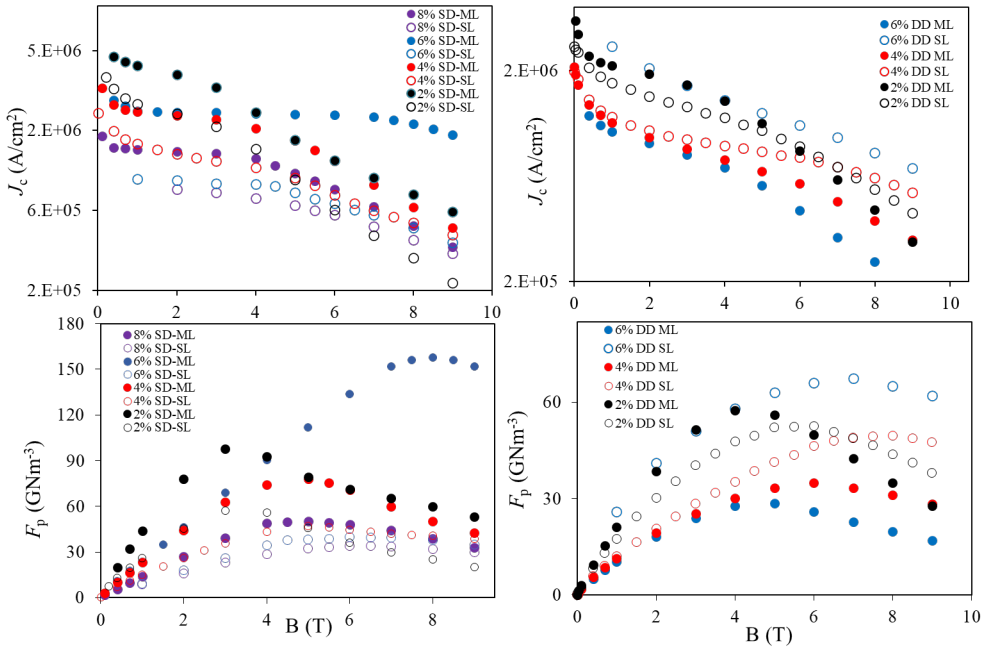

Figure 3. J_c(B) curves measured on (a) BZO/YBCO SD-SL and SD-ML, and (b) 2-6% BZO/YBCO DD-SL and DD-ML films at 65 K. F_p (B) curves measured on the (c) BZO/YBCO SD-SL and SD-ML and (d) 2-6% BZO/YBCO DD-SL and DD-ML films at 65 K with B//c-axis.

As a further confirmation of the extension of improved pinning beyond B//c in ML films, Figure 4a-4b compares the $J_c(\theta)$ 65K data for the selected samples in Figure 3. The solid and open symbols correspond to the ML and SL films respectively. In Figure 4a, the J_c (θ) of 2% BZO/YBCO SD-SL (open) and BZO/YBCO SD-ML (solid) are compared at B=5 T (black) and 9.0 T (red). Essentially, the ML film has higher J_c than its corresponding SL sample over the entire θ range. Case in point, the maximum $J_c(\theta \leq 85^o)$ of 2% ML sample is almost double and about 1.5 times that of the 2% SL film at 5.0 T and 9.0 T respectively. J_c (θ) enhancement is even more pronounced at a higher BZO doping of 6% shown in Figure 4b. In the range $\theta \leq 85^o$, enhancement factors as high as 2.8 and 4.5 are seen at 5.0 T and 9.0 T respectively. It should be noted that the enhanced pinning is not only limited to B/c-axis while the highest enhancement factors along B//c of 1.7 and 4.4 for the 2% ML and 6% ML respectively. With increasing θ, the J_c enhancement decreases monotonically and drops to ~ 1.0 and 1.5 respectively ~ 67°. In DD case, enhanced J_c in ML sample as compared to its SL counterpart's in a broad angular range has also been observed at low BZO doping of 2% case (Figure 4c). At 5.0 T, the enhancement is

across the entire angular range. However, the enhancement is larger at B//ab-plane by a factor of 1.8. At 9.0 T, the $J_c(\theta)$ curves for the DD-SL and DD-ML samples cross at ~ θ~30 degree. At higher BZO doping of 6%, the $J_c(\theta)$ curve for the DD-SL is higher than its DD-ML counterpart's across the entire angular range (Figure 4d).

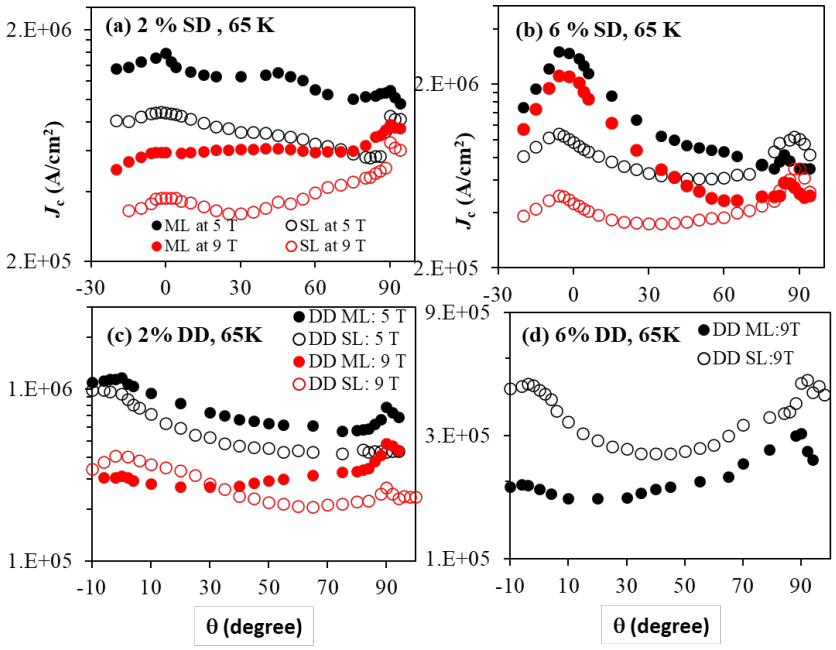

Figure 4. $J_c(\theta)$ curves taken at 65 K on (a) 2% BZO/YBCO SD-SL (open) and SD-ML (solid), (b) 6% BZO/YBCO SD-SL (open) and SD-ML (solid), (c) 2% BZO/YBCO DD-SL (open) and DD-ML (solid), and (d) 6% BZO/YBCO DD-SL (open) and DD-ML (solid) films at selected magnetic fields.

4. Conclusions

In summary, through this comparative study of four sets of BZO/YBCO samples, we probe the role of Ca in BZO/YBCO nanocomposites in improving the pinning efficiency of BZO 1D-APCs. A few interesting insights have been obtained. First, the comparison between the BZO/YBCO SD-SL and SD-ML samples has revealed enhanced $J_c(B)$ and $F_p(B)$ for BZO doping in the range of 2-8 vol.% in the latter in most B field range up to 9.0 T. Since the only difference between the two sets is the presence of the two 10 nm thick CaY-123 spacers that do not affect the BZO 1D-APC diameter and concentration except truncate them into ~segments aligned still in the c-axis, Ca diffusion from these spacers into BZO/YBCO leads to the enhanced pinning. Microscopically, Ca/Y, Ca/Ba and Ca/Cu are all possible replacements in YBCO. Considering Ca ion has a comparable size to Y ion while is 30% smaller (larger) than Ba (Cu) ion, Ca/Y replacement is energetically favored in YBCO under negligible strain field. In contrast, Ca/Ba (or Ca/Cu) replacement would be favorable in YBCO under compressive (or tensile strain). This means Cu/Ca replacement would most likely occur at the BZO/YBCO interface where the tensile strain initiated from the large BZO/YBCO lattice mismatch is the highest. This has been confirmed in BZO/YBCO SD-ML samples and the Ca/Cu replacement leads to elongation of the c-axis of YBCO with significantly reduced lattice mismatch and hence coherent BZO/YBCO interface. Away from this interface, Ca/Y replacement may dominate, resulting in reduced T_c values, which has been confirmed in all ML samples. When the modulated strain field is disturbed in DD samples, especially when the long-range tensile strain along the BZO/YBCO interface is interrupted in the mixed APC landscape, Ca/Y replacement may become dominant overweighing the benefit of Ca-repair on the BZO/YBCO interface, the enhanced pinning is limited to low BZO doping where tensile-strain directed Ca diffusion along the BZO/YBCO interface is still present. This result illustrates the importance of a

coherent APC/YBCO interface for optimal pinning efficiency and the need for further exploration of approaches to achieve such in complex pinning landscape required for practical applications.

5. References

1. Wu, J. and J. Shi, *Interactive modeling-synthesis-characterization approach towards controllable in situ self-assembly of artificial pinning centers in RE-123 films.* Superconductor Science & Technology, 2017. **30**(10).
2. Shi, J.J. and J.Z. Wu, *Micromechanical model for self-organized secondary phase oxide nanorod arrays in epitaxial YBa2Cu3O7− δ films.* Philosophical Magazine, 2012. **92**(23): p. 2911-2922.
3. Shi, J.J. and J.Z. Wu, *Influence of the lattice strain decay on the diameter of self assembled secondary phase nanorod array in epitaxial films.* Journal of Applied Physics, 2015. **118**(16).
4. Baca, F.J., et al., *Interactive Growth Effects of Rare-Earth Nanoparticles on Nanorod Formation in YBa2Cu3Ox Thin Films.* Advanced Functional Materials, 2013. **23**(38): p. 4826-4831.
5. Chen, S., et al., *Enhancement of isotropic pinning force in YBCO films with BaZrO3 nanorods and Y2O3 nanoparticles.* IEEE Trans. Appl. Supercond, 2017. **27**(4): p. 4-8.
6. MacManus-Driscoll, J., et al., *Strongly enhanced current densities in superconducting coated conductors of YBa 2 Cu 3 O 7–x+ BaZrO 3.* Nature materials, 2004. **3**(7): p. 439.
7. Matsumoto, K. and P. Mele, *Artificial pinning center technology to enhance vortex pinning in YBCO coated conductors.* Superconductor Science and Technology, 2009. **23**(1): p. 014001.
8. Wee, S.H., et al., *Engineering nanocolumnar defect configurations for optimized vortex pinning in high temperature superconducting nanocomposite wires.* Scientific Reports, 2013. **3**: p. 2310.
9. Mele, P., et al., *Ultra-high flux pinning properties of BaMO3-doped YBa2Cu3O7− x thin films (M= Zr, Sn).* Superconductor Science and Technology, 2008. **21**(3): p. 032002.
10. Varanasi, C., et al., *Thick YBa 2 Cu 3 O 7− x+ BaSnO 3 films with enhanced critical current density at high magnetic fields.* Applied Physics Letters, 2008. **93**(9): p. 092501.
11. Gautam, B., et al., *Microscopic adaptation of BaHfO3 and Y2O3 artificial pinning centers for strong and isotropic pinning landscape in YBa2Cu3O7–x thin films.* Superconductor Science and Technology, 2018. **31**(2): p. 025008.
12. Matsushita, T., *Flux pinning in superconducting 123 materials.* Superconductor Science and Technology, 2000. **13**(6): p. 730.
13. Miura, S., et al., *Characteristics of high-performance BaHfO3-doped SmBa2Cu3Oy superconducting films fabricated with a seed layer and low-temperature growth.* Superconductor Science and Technology, 2015. **28**(6): p. 065013.
14. Sebastian, M.A.P., et al., *Study of the Flux Pinning Landscape of YBCO Thin Films With Single and Mixed Phase Additions BaMO3+ Z: M= Hf, Sn, Zr and Z= Y2O3, Y211.* IEEE Transactions on Applied Superconductivity, 2017. **27**(4): p. 1-5.
15. Tobita, H., et al., *Fabrication of BaHfO3 doped Gd1Ba2Cu3O7− δ coated conductors with the high Ic of 85 A/cm-w under 3 T at liquid nitrogen temperature (77 K).* Superconductor Science and Technology, 2012. **25**(6): p. 062002.

16. Feldmann, D., et al., *Improved flux pinning in YBa2Cu3O7 with nanorods of the double perovskite Ba2YNbO6.* Superconductor Science and Technology, 2010. **23**(9): p. 095004.
17. Opherden, L., et al., *Large pinning forces and matching effects in YBa 2 Cu 3 O 7-δ thin films with Ba 2 Y (Nb/Ta) O 6 nano-precipitates.* Scientific reports, 2016. **6**: p. 21188.
18. Foltyn, S., et al., *Materials science challenges for high-temperature superconducting wire.* Nature materials, 2007. **6**(9): p. 631.
19. Gautam, B., et al., *Probing the effect of interface on vortex pinning efficiency of one-dimensional BaZrO3 and BaHfO3 artificial pinning centers in YBa2Cu3O7-x thin films.* Applied Physics Letters, 2018. **113**(21): p. 212602.
20. Wu, J., et al., *Pinning Efficiency of One-Dimensional Artificial Pinning Centers in YBa 2 Cu 3 O 7-x Thin Films*. Vol. 29. 2019. 1-5.
21. Cantoni, C., et al., *Strain-driven oxygen deficiency in self-assembled, nanostructured, composite oxide films.* ACS nano, 2011. **5**(6): p. 4783-4789.
22. Blatter, G., et al., *Vortices in high-temperature superconductors.* Reviews of Modern Physics, 1994. **66**(4): p. 1125.
23. Ogunjimi, V., et al. *The effect of APC/YBCO interface on the angular range of effective pinning by one-dimensional artificial pinning centers in YBa2Cu3O7-x nanocomposite films*. in *IOP Conference Series: Materials Science and Engineering*. 2020. IOP Publishing.
24. Ogunjimi, V., et al., *The angular range of effective pinning by one-dimensional artificial pinning centers in BaZrO3/YBa2Cu3O7-x nanocomposite films.* AIP Advances, 2019. **9**(8): p. 085110.
25. Ogunjimi, V., et al., *Enhancing Magnetic Pinning by BaZrO3 Nanorods Forming Coherent Interface by Strain-Directed Ca-doping in YBa2Cu3O7-x Nanocomposite Films.* Superconductor Science and Technology, 2021.
26. Wu, J.Z., et al., *Enabling coherent BaZrO3 nanorods/YBa2Cu3O7− x interface through dynamic lattice enlargement in vertical epitaxy of BaZrO3/YBa2Cu3O7− x nanocomposites.* Superconductor Science and Technology, 2022. **35**(3): p. 034001.
27. Klie, R.F., et al., *Enhanced current transport at grain boundaries in high-T-c superconductors.* Nature, 2005. **435**(7041): p. 475-478.
28. Baca, F.J., et al., *Control of BaZrO(3) nanorod alignment in YBa(2)Cu(3)O(7-x) thin films by microstructural modulation.* Applied Physics Letters, 2009. **94**(10): p. 3.
29. Sebastian, M.A., et al., *Comparison Study of the Flux Pinning Enhancement of YBa2Cu3O7−δ Thin Films With BaHfO3 + Y2O3 Single- and Mixed-Phase Additions.* IEEE Transactions on Applied Superconductivity, 2019. **29**(5): p. 1-5.
30. Wang, X., et al., *Eliminating thickness dependence of critical current density in YBa2Cu3O7-x films with aligned BaZrO3 nanorods.* Journal of Applied Physics, 2010. **108**(11): p. 3911.
31. Chen, S., et al., *Enhancement of Isotropic Pinning Force in YBCO Films With BaZrO3 Nanorods and Y2O 3 Nanoparticles.* IEEE Transactions on Applied Superconductivity, 2017. **27**(4): p. 1-5.
32. Gautam, B., et al., *Microscopic Adaptation of BaHfO3 and Y2O3 Artificial Pinning Centers for Strong and Isotropic Pinning Landscape in YBa2Cu3O7-x Thin Films.* Superconductor Science and Technology, 2017.
33. Emergo, R.L.S., et al., *The effect of thickness and substrate tilt on the BZO splay and superconducting properties of YBa2Cu3O7 − δfilms.* Superconductor Science and Technology, 2010. **23**(11): p. 115010.

34. Baca, F., et al., *Control of BaZrO3 nanorod alignment in YBa2Cu3O7-x thin films by microstructural modulation.* Applied Physics Letters, 2009. **94**(10): p. 2512.
35. Chen, S., et al., *Generating mixed morphology BaZrO3 artificial pinning centers for strong and isotropic pinning in BaZrO3–Y2O3 double-doped YBCO thin films.* Superconductor Science and Technology, 2017. **30**(12): p. 125011.
36. Horide, T., M. Ishimaru, and K. Matsumoto, *Observation of inhomogeneous depinning in YBa2Cu3O7 composite multilayers.* Superconductor Science and Technology, 2019. **32**(8): p. 085001.
37. Horide, T., et al., *Hybrid artificial pinning centers of elongated-nanorods and segmented-nanorods in Yba2Cu3O7 films.* Superconductor Science and Technology, 2016. **29**(10): p. 105010.
38. Malmivirta, M., et al., *Enhanced flux pinning in YBCO multilayer films with BCO nanodots and segmented BZO nanorods.* Scientific reports, 2017. **7**(1): p. 1-8.
39. Horide, T., et al., *Structural Evolution Induced by Interfacial Lattice Mismatch in Self-Organized YBa2Cu3O7− δ Nanocomposite Film.* ACS nano, 2017. **11**(2): p. 1780-1788.
40. Shi, J.J. and J.Z. Wu, *Structural transition of secondary phase oxide nanorods in epitaxial YBa2Cu3O7− δ films on vicinal substrates.* Philosophical Magazine, 2012. **92**(34): p. 4205-4214.
41. Wu, J. and J. Shi, *Interactive modeling-synthesis-characterization approach towards controllable in situ self-assembly of artificial pinning centers in RE-123 films.* Superconductor Science and Technology, 2017. **30**(10): p. 103002.
42. Wu, J.Z., et al., *The effect of lattice strain on the diameter of BaZrO3 nanorods in epitaxial YBa2Cu3O7− δ films.* Superconductor Science and Technology, 2014. **27**(4): p. 044010.
43. Yoshida, Y., et al., *Approaches in controllable generation of artificial pinning center in REBa2Cu3Oy-coated conductor for high-flux pinning.* Superconductor Science and Technology, 2017. **30**(10): p. 104002.
44. Huhtinen, H., et al., *The effect of BZO doping concentration and thickness dependent properties of YBCO films grown by PLD on buffered NiW substrates.* Physica C: Superconductivity, 2012. **472**(1): p. 66-74.
45. Huhtinen, H., et al., *Influence of BaZrO 3 dopant concentration on properties of YBa 2 Cu 3 O 6+ x films in magnetic fields up to 30 T.* Journal of Applied Physics, 2010. **107**(5): p. 053906.
46. Jha, A.K., et al., *Tailoring the vortex pinning strength of YBCO thin films by systematic incorporation of hybrid artificial pinning centers.* Superconductor Science and Technology, 2015. **28**(11): p. 114004.

Acknowledgement
This research was supported in part by NSF contracts Nos: NSF-DMR-1909292, the AFRL Aerospace Systems Directorate, the Air Force Office of Scientific Research (AFOSR) LRIR #14RQO8COR and LRIR #18RQCOR100. D.Z. and H.W. acknowledge the support from the U.S. National Science Foundation for the high-resolution STEM effort at Purdue University (DMR-2016453).